SINGLE IMAGE SUPER-RESOLUTION OF MEDICAL ULTRASOUND IMAGES USING A FAST ALGORITHM

Ningning Zhao[1,2], Qi Wei[3], Adrian Basarab[2], Denis Kouamé [2], Jean-Yves Tourneret[1]

[1] University of Toulouse, IRIT/INP-ENSEEIHT, 31071 Toulouse Cedex 7, France
[2] University of Toulouse, IRIT, CNRS UMR 5505, Université Paul Sabatier, Toulouse, France
[3] University of Cambridge, Department of engineering, UK
{nzhao, jean-yves.tourneret}@enseeiht.fr, {qw245}@cam.ac.uk, {adrian.basarab, denis.kouame}@irit.fr

ABSTRACT

This paper addresses the problem of super-resolution (SR) for medical ultrasound (US) images. Contrary to device-based approaches, we investigate a post-processing method to invert the direct linear model of US image formation. Given the ill-posedness of single image SR, we proposed an ℓ_p-norm ($1 \leq p \leq 2$) regularizer for the US tissue reflectivity function/image to be estimated. To solve the associated optimization problem, we propose a novel way to explore the decimation and blurring operators simultaneously. As a consequence, we are able to compute the analytical solution for the ℓ_2-norm regularized SR problem and to embed the analytical solution to an alternating direction method of multipliers for the ℓ_p-norm regularized SR problem. The behavior of the proposed algorithm is illustrated using synthetic, simulated and *in vivo* US data.

Index Terms— Ultrasound, single image super-resolution, circulant matrix, ADMM, ℓ_p-norm regularization.

1. INTRODUCTION

Medical ultrasound imaging (USI) has been widely used for clinical diagnosis, especially for soft tissue applications including cardiovascular medicine and obstetrics [1]. USI has many advantages compared to other medical imaging modalities such as X-ray computed tomography and magnetic resonance imaging including its harmless, cost-effective, portable and noninvasive properties. However, US images suffer from a relatively low contrast, reduced spatial resolution and low signal-to-noise ratio. Even though advances in ultrasonic hardware have improved the resolution of US images during the last 15-20 years, e.g., [1, 2], post-processing techniques enhancing US image resolution are still appealing due to the physical limitations of device-based solutions. In an ultrasound system, there are
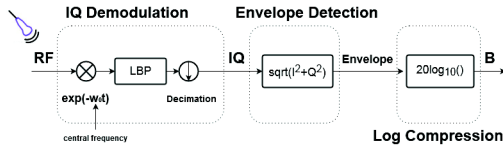

Fig. 1. Relationship between different US image modes.

basically three image modes available for analysis, including *radio-*

frequency (RF) data, *in phase/quadrature* (IQ) data and B-mode image (also called displayed image) [3], whose relationships are shown in Fig. 1. In this work, we focus on the complex IQ data. Due to the linearity of the demodulation process, the convolution model classically used for RF data can be used to describe the IQ image formation [4]. This model is defined as

$$\mathbf{y} = \mathbf{SHx} + \mathbf{n} \qquad (1)$$

where the vector $\mathbf{y} \in \mathbb{C}^{N_l \times 1}$ ($N_l = m_l \times n_l$) is the observation and $\mathbf{x} \in \mathbb{C}^{N_h \times 1}$ ($N_h = m_h \times n_h$) is the vectorized tissue reflectivity function (TRF), i.e., the image to be estimated, with $N_h > N_l$. These vectors are obtained by stacking the corresponding images into column vectors using a lexicographic order. The vector $\mathbf{n} \in \mathbb{C}^{N_l \times 1}$ is classically supposed to be an independent identically distributed (*i.i.d.*) additive white Gaussian noise (AWGN). The matrices $\mathbf{S} \in \mathbb{R}^{N_l \times N_h}$ and $\mathbf{H} \in \mathbb{C}^{N_h \times N_h}$ are associated with the decimation and blurring/convolution operators. More specifically, $\mathbf{H}$ is a block circulant matrix with circulant blocks (BCCB) corresponding to cyclic convolution boundaries, and left multiplying by $\mathbf{S}$ corresponds to down-sampling with an integer factor d ($d = d_r \times d_c$), with the relationships $N_h = N_l \times d$, $m_h = m_l \times d_r$ and $n_h = n_l \times d_c$.

The US image super-resolution (SR) problem consists of estimating the TRF vector $\mathbf{x}$ from the observation vector $\mathbf{y}$, which requires additional prior information to regularize this well-known ill-posed problem. An ℓ_2-norm regularized method is known to produce over-smoothed results, the TV regularized method produces piece-wise smoothing results, whereas the ℓ_1-norm regularizer can be used when the solution is known to be sparse [5]. In this paper, we consider an ℓ_p-norm regularizer with $1 \leq p \leq 2$ for the TRF $\mathbf{x}$, which obviously generalizes the ℓ_1-norm and ℓ_2-norm regularizers [6, 7].

The single image SR problem was solved in [8] with the alternating direction method of multipliers (ADMM) by separating the SR problem into up-sampling and deconvolution steps that can be solved efficiently and iteratively. First order gradient-based algorithms were also investigated for the image SR problem in [9]. However, these algorithms assume that the function to be optimized is differentiable, which limits their applications. In this paper, we propose to handle the decimation and blurring matrices simultaneously by exploring their specific properties in the Fourier domain [10]. Note that similar properties were mentioned in [11, 12] in different contexts.

2. PROPOSED SUPER-RESOLUTION ALGORITHM

2.1. Problem formulation

Similar to the traditional image reconstruction problems, accounting for the AWGN and the prior information for the TRF, we consider

the following optimization problem

$$\min_{\mathbf{x}} \frac{1}{2}\|\mathbf{y} - \mathbf{SHx}\|_2^2 + \tau\|\mathbf{x}\|_p^p \quad (2)$$

where $\|\mathbf{x}\|_p = \sqrt[p]{|x_1|^p + \cdots |x_{N_h}|^p}$ is the ℓ_p-norm and τ is the regularization parameter balancing the weights of the data fidelity and regularization terms. Under the cyclic boundary assumption, the blurring matrix $\mathbf{H}$ is diagonalizable in the Fourier domain leading to

$$\mathbf{H} = \mathbf{F}^H \mathbf{\Lambda} \mathbf{F} \quad \text{and} \quad \mathbf{H}^H = \mathbf{F}^H \mathbf{\Lambda}^H \mathbf{F} \quad (3)$$

where $\mathbf{F}/\mathbf{F}^H$ are the Fourier and inverse Fourier transform operators and $\mathbf{\Lambda} = \operatorname{diag}\{\mathbf{Fh}\}$, where $\mathbf{h}$ is the first column of the matrix $\mathbf{H}$.

2.2. Estimation of the TRF x

As mentioned in the introduction, we propose to handle the decimation and blurring matrices simultaneously by taking into account the properties of the decimation matrix in the Fourier domain. More precisely, the following result can be obtained [12]

$$\mathbf{F}\underline{\mathbf{S}}\mathbf{F}^H = \frac{1}{d}\mathbf{J}_d \otimes \mathbf{I}_{N_l} \quad (4)$$

where $\mathbf{J}_d \in \mathbb{R}^{d\times d}$ is a matrix of ones, $\mathbf{I}_{N_l} \in \mathbb{R}^{N_l\times N_l}$ is the identity matrix, $\underline{\mathbf{S}} = \mathbf{S}^H\mathbf{S}$ and $\otimes$ is the Kronecker product. Using (4), an analytical solution to (2) for $p = 2$ is

$$\mathbf{x} = (\mathbf{H}^H\mathbf{S}^H\mathbf{SH} + 2\tau\mathbf{I}_{N_h})^{-1}\mathbf{r}$$
$$= \mathbf{F}^H(\mathbf{\Lambda}^H\mathbf{F}\underline{\mathbf{S}}\mathbf{F}^H\mathbf{\Lambda} + 2\tau\mathbf{I}_{N_h})^{-1}\mathbf{Fr} \quad (5)$$

where $\mathbf{r} = \mathbf{H}^H\mathbf{S}^H\mathbf{y}$. The computation of (5) is complicated due to the huge and non-diagonalizable matrix to be inverted. The existing methods to solve this problem include iterative optimization [8] and sampling [13] methods that are still computationally intensive. The main contribution of this paper is the derivation of the analytical solution (5) (i.e., the solution of (2) for $p = 2$) presented in Theorem 1.

Theorem 1. *The solution of* (5) *can be computed as*

$$\hat{\mathbf{x}} = \frac{1}{2\tau}\mathbf{r} - \frac{1}{2\tau}\mathbf{F}^H\underline{\mathbf{\Lambda}}^H\left(2\tau d\mathbf{I}_{N_l} + \underline{\mathbf{\Lambda}}\underline{\mathbf{\Lambda}}^H\right)^{-1}\underline{\mathbf{\Lambda}}\mathbf{Fr} \quad (6)$$

where $\underline{\mathbf{\Lambda}} = (\underbrace{\mathbf{I}_{N_l}, \cdots, \mathbf{I}_{N_l}}_{d})\mathbf{\Lambda} \in \mathbb{C}^{N_l\times N_h}$.

Proof. Use the Woodbury inversion lemma, see [10] for more details of the proof. □

Moreover, the analytical solution (6) can be embedded into an ADMM framework for $1 \leqslant p < 2$. Precisely, by introducing an additional variable $\mathbf{u} = \mathbf{x}$, (2) can be rewritten as

$$\min_{\mathbf{x},\mathbf{u}} \quad \frac{1}{2}\|\mathbf{y} - \mathbf{SHx}\|_2^2 + \tau\|\mathbf{u}\|_p^p$$
$$\text{subject to} \quad \mathbf{u} = \mathbf{x}. \quad (7)$$

The augmented Lagrangian function associated with (7) is

$$L(\mathbf{x},\mathbf{u},\boldsymbol{\lambda}) = \frac{1}{2}\|\mathbf{y} - \mathbf{SHx}\|_2^2 + \tau\|\mathbf{u}\|_P^p + \boldsymbol{\lambda}^T(\mathbf{x}-\mathbf{u}) + \frac{\mu}{2}\|\mathbf{x}-\mathbf{u}\|_2^2$$

or equivalently

$$L(\mathbf{x},\mathbf{u},\mathbf{d}) = \frac{1}{2}\|\mathbf{y} - \mathbf{SHx}\|_2^2 + \tau\|\mathbf{u}\|_P^p + \frac{\mu}{2}\|\mathbf{x}-\mathbf{u}+\mathbf{d}\|_2^2 \quad (8)$$

where $\mathbf{d} = (1/\mu)\boldsymbol{\lambda}$ is the scaled dual variable with $\mu > 0$. Then, the problem (8) can be solved iteratively as

For $k = 0,\dots$
$$\begin{vmatrix} \mathbf{x}_{k+1} \in \operatorname{argmin}_{\mathbf{x}} \frac{1}{2}\|\mathbf{y} - \mathbf{SHx}\|_2^2 + \frac{\mu}{2}\|\mathbf{x} - \mathbf{u}_k + \mathbf{d}_k\|_2^2 \\ \mathbf{u}_{k+1} \in \operatorname{argmin}_{\mathbf{u}} \tau\|\mathbf{u}\|_p^p + \frac{\mu}{2}\|\mathbf{x}_{k+1} - \mathbf{u} + \mathbf{d}_k\|_2^2 \\ \mathbf{d}_{k+1} = \mathbf{d}_k + (\mathbf{x}_{k+1} - \mathbf{u}_{k+1}) \end{vmatrix}$$
$$(9)$$

The optimization problems w.r.t. $\mathbf{x}$ and $\mathbf{u}$ involved in (9) are detailed below

- Update $\mathbf{x}$: The analytical solution of the MAP estimator of $\mathbf{x}$ can be calculated as follows

$$\mathbf{x}_{k+1} = (\mathbf{H}^H\mathbf{S}^H\mathbf{SH} + \mu\mathbf{I}_{N_h})^{-1}\mathbf{r}_1$$
$$= \mathbf{F}^H(\mathbf{\Lambda}^H\mathbf{F}\underline{\mathbf{S}}\mathbf{F}^H\mathbf{\Lambda} + \mu\mathbf{I}_{N_h})^{-1}\mathbf{Fr}_1 \quad (10)$$

  where $\mathbf{r}_1 = \mathbf{H}^H\mathbf{S}^H\mathbf{y} + \mu(\mathbf{u}_k - \mathbf{d}_k)$. Theorem 1 can be finally used to compute the solution (10).

- Update $\mathbf{u}$: The MAP estimator of $\mathbf{u}$ can be calculated with the following proximal operator since $\mathbf{u}$ is pixel-wise decoupled [14]

$$\operatorname{prox}_{|\cdot|^p}(\nu) = \operatorname{argmin}_u \tau|u|^p + \frac{\mu}{2}|\nu - u|^2 \quad (11)$$

  where ν is an element from the vector $\boldsymbol{\nu} = \mathbf{x}_{k+1} + \mathbf{d}_k$. Note that when p belongs to $\{1, 4/3, 3/2, 2\}$, the analytical solution of the proximal operator (11) can be found in [14].

2.3. Proposed algorithm

The SR algorithm resulting from the previous derivations is summarized in Algo. 1. Note that the regularization parameters used in this paper have been adjusted manually by cross-validation.
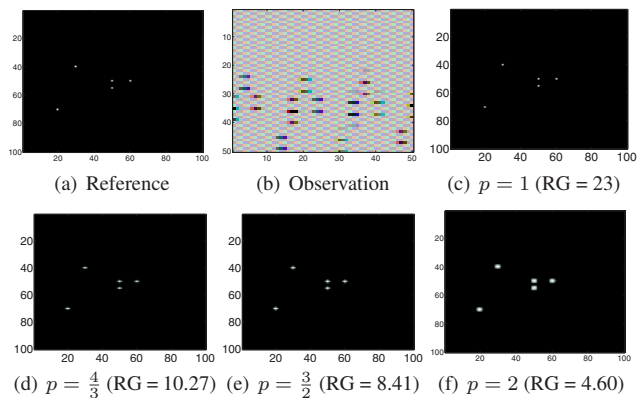

Algorithm 1: fast SR algorithm for US images

1 Set $k = 0$, choose $\mu > 0, \tau > 0, \mathbf{x}_0, \mathbf{d}_0$;
2 Repeat
   // 1) Update **x** using (10)
3 $\mathbf{r}_1 = \mathbf{H}^H\mathbf{S}^H\mathbf{y} + \mu(\mathbf{u}_k - \mathbf{d}_k)$;
4 $\mathbf{\Lambda} \leftarrow \operatorname{Dec}(\mathbf{H})$;
5 $\underline{\mathbf{\Lambda}} \leftarrow \mathbf{\Lambda}\mathbf{\Lambda}^H$;
6 $\mathbf{x}_f \leftarrow \left(\underline{\mathbf{\Lambda}}^H\left(\mu d\mathbf{I}_{N_l} + \underline{\mathbf{\Lambda}}\underline{\mathbf{\Lambda}}^H\right)^{-1}\underline{\mathbf{\Lambda}}\right)\mathbf{Fr}_1$;
7 $\mathbf{x}_{k+1} \leftarrow \frac{1}{\mu}\mathbf{r}_1 - \frac{1}{\mu}\mathbf{F}^H\mathbf{x}_f$;
   // 2) Update **u** using the proximal operator
8 $\boldsymbol{\nu} = \mathbf{x}_{k+1} + \mathbf{d}_k$;
9 $\mathbf{u}_{k+1} = \operatorname{prox}_{|\cdot|^p}(\boldsymbol{\nu})$;
   // 3) Update the dual variables **d**
10 $\mathbf{d}_{k+1} = \mathbf{d}_k + (\mathbf{x}_{k+1} - \mathbf{u}_{k+1})$;
11 $k \leftarrow k + 1$
12 until stopping criterion is satisfied.

---

3. SIMULATION RESULTS

In this section, we evaluate the proposed algorithm on synthetic data, simulated and *in vivo* US images. The performance of the algorithms is assessed using the resolution gain (RG), whose definition is the ratio of the normalized auto-correlation (higher than 3 dB) of the interpolation of the observed US data to the normalized auto-correlation (higher than 3 dB) of the restored TRF. Note that RG is widely used in US image reconstruction problems [5, 15].

3.1. Synthetic data

We first tested the proposed algorithm on synthetic data, as shown in Fig. 2 (a)-(b). The synthetic sparse data (isolated Diracs) was convolved by a PSF represented by a Gaussian function modulated by a 3.4 MHz cosine sampled at a rate of 20 MHz. Note that the observations have been scaled for better visualization in this paper (i.e., the LR images contain d times fewer pixels than the corresponding HR images). In this group of experiments, we studied the efficiency of the ℓ_p-norm regularizer for $p \in \{1, 4/3, 3/2, 2\}$. The regularization parameter τ was set to 0.001 and the decimation factors were $d_r = d_c = 2$. The restored images and the numerical RG results are reported in Fig. 2 (c)-(f). As illustrated in Fig. 2, the smaller the value of p is, the higher RG we can obtain. The results are coherent since the ℓ_1-norm regularized problem favors a sparse solution.

| (a) Reference | (b) Observation | (c) $p = 1$ (RG = 23) |

| (d) $p = \frac{4}{3}$ (RG = 10.27) | (e) $p = \frac{3}{2}$ (RG = 8.41) | (f) $p = 2$ (RG = 4.60) |

Fig. 2. Synthetic data and SR results with the proposed method with ℓ_p-norm regularization terms.

3.2. Simulated US image

This section evaluates the performance of the proposed algorithm on simulated images of size 78×88, as shown in Fig. 3 (a)-(c). The observation (Fig. 3 (a)) has been generated from the decimation of the convolution between a TRF of size 156×196 (Fig. 3 (c)) and a standard US PSF with decimation factors $d_r = d_c = 2$. The regularization parameter is $\tau = 0.0001$. The restored images using ℓ_p-norm regularization terms with the proposed algorithm are shown in Fig. 3 (e)-(h). The corresponding numerical results are reported in Table 1. Compared to the synthetic data in Section 3.1, the simulated US image is not sparse explaining why the restored image using the ℓ_p-norm regularizer with $p = 4/3$ outperforms the others. Thus, we emphasize that the choice of the value of p highly depends on the statistical properties of the TRF. Furthermore, we also show that our method outperforms, in terms of RG, the super-resolution technique introduced in [8] using a TV regularizer (see Fig. 3 (d)).
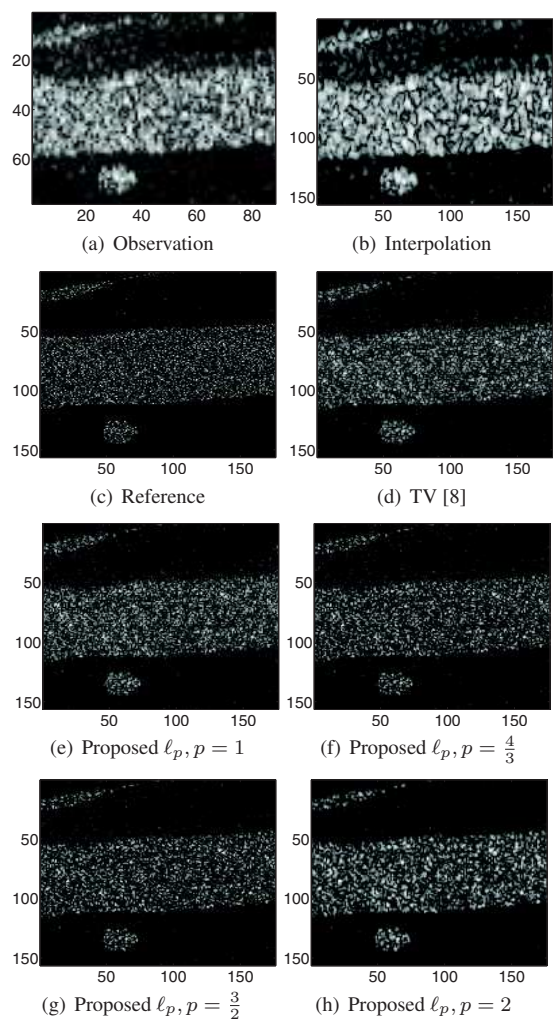
3.3. *In vivo* US image

Finally, the proposed SR algorithm was tested on *in vivo* US data using ℓ_p-norm regularization. The image displayed in Fig. 4 (a) is a mouse kidney image acquired with a probe of 25MHz central frequency. We carried out SR experiments on the region located inside the red box, shown in Fig.4 (b). The up-sampling factors were set to $d_r = d_c = 2$. The PSF was estimated directly from the data following [16]. Finally, the regularization parameter τ was set to 0.1 in this section. For the real data, we compared the proposed

algorithm with a classical ADMM implementation [8, 10] [1]. The restored images obtained with the proposed method are shown in Fig. 4 (c)-(f), while the ones estimated with the classical method are shown in Fig. 4 (g)-(j). The numerical results are reported in Table 2. According to the graphical and numerical results, the restored images with the proposed algorithm and the classical method are similar in terms of RG. However, the proposed algorithm needs less CPU time and a reduced number of iterations (when compared to the classical method) to converge.

Table 1. SR of the simulated US image

Prior ℓ_p	RG	Time (s)	Iters.
$p = 2$	2.37	0.004	-
$p = 1$	9.56	1.55	317
$p = 4/3$	**26.01**	2.98	300
$p = 3/2$	22.63	2.20	329
TV [8]	2.24	2.70	289

| (a) Observation | (b) Interpolation |

| (c) Reference | (d) TV [8] |

| (e) Proposed $\ell_p, p = 1$ | (f) Proposed $\ell_p, p = \frac{4}{3}$ |

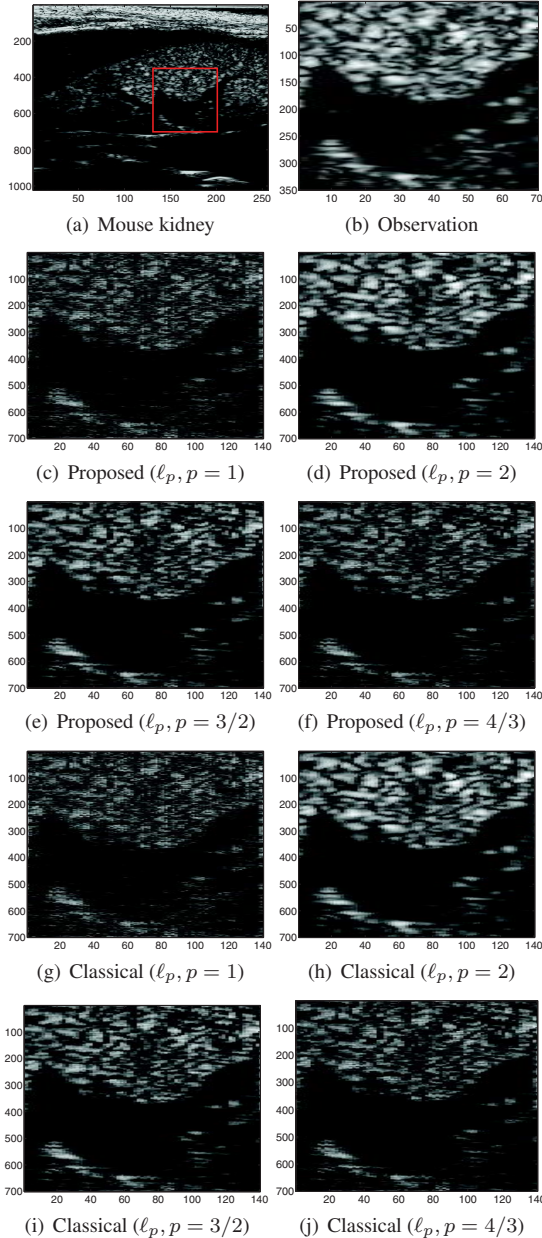| (g) Proposed $\ell_p, p = \frac{3}{2}$ | (h) Proposed $\ell_p, p = 2$ |

Fig. 3. Simulated US image and the SR results using ℓ_p-norm and TV regularizers.

---

[1]The classical method needs to split the SR problem into deconvolution and up-sampling problems.

Table 2. SR of the real US image

ℓ_p	Method	RG	Time (s)	Iters.
$p = 2$	Proposed	1.78	**0.009**	-
	Classical	1.78	0.53	55
$p = 1$	Proposed	**16.26**	**2.42**	190
	Classical	**16.50**	2.58	199
$p = \frac{4}{3}$	Proposed	9.72	**0.76**	28
	Classical	10.04	1.12	37
$p = \frac{3}{2}$	Proposed	5.55	**0.31**	14
	Classical	5.72	0.75	33

(a) Mouse kidney

(b) Observation

(c) Proposed (ℓ_p, $p = 1$)

(d) Proposed (ℓ_p, $p = 2$)

(e) Proposed (ℓ_p, $p = 3/2$)

(f) Proposed (ℓ_p, $p = 4/3$)

(g) Classical (ℓ_p, $p = 1$)

(h) Classical (ℓ_p, $p = 2$)

(i) Classical (ℓ_p, $p = 3/2$)

(j) Classical (ℓ_p, $p = 4/3$)

Fig. 4. *In vivo* US image and the restored images with the proposed and classical methods using ℓ_p norm regularizers.

4. CONCLUSION

This paper studied a new super-resolution algorithm for ultrasound images. By exploring the properties of the decimation matrix in the Fourier domain, we were able to calculate an analytical solution of the super-resolution problem with an ℓ_2-norm regularizer and were able to embed this analytical solution into an ADMM framework for a more general ℓ_p-norm regularizer ($p \in [1, 2]$). Due to the implementation of the analytical solution, the proposed method allowed to reduce the computation time comparing with the classical method. Our results also showed that better restoration performance can be obtained with the ℓ_p-norm regularizer, depending on the image structure.

5. REFERENCES

[1] M. Tanter and M. Fink, "Ultrafast imaging in biomedical ultrasound," *IEEE Trans. Ultrason. Ferroelectr. Freq. Control*, vol. 61, no. 1, pp. 102–119, 2014.

[2] M. A. Ellis, F. Viola, and W. F. Walker, "Super-resolution image reconstruction using diffuse source models," *Ultrasound in Med. and Bio.*, vol. 36, no. 6, pp. 967–977, 2010.

[3] J. Kirkhorn, "Introduction to IQ-demodulation of RF-data," IFBT, NTNU, Tech. Rep., 1999.

[4] O. Michailovich and A. Tannenbaum, "Blind deconvolution of medical ultrasound images: A parametric inverse filtering approach," *IEEE Trans. Image Process.*, vol. 16, no. 12, pp. 3005–3019, 2007.

[5] C. Yu, C. Zhang, and L. Xie, "An envelope signal based deconvolution algorithm for ultrasound imaging," *Signal Processing*, vol. 92, no. 3, pp. 793 – 800, 2012.

[6] M. Alessandrini, S. Maggio, J. Poree, L. D. Marchi, N. Speciale, E. Franceschini, O. Bernard, and O. Basset, "A restoration framework for ultrasonic tissue characterization," *IEEE Trans. Ultrason. Ferroelectr. Freq. Control*, vol. 58, no. 11, pp. 2344–2360, 2011.

[7] N. Zhao, A. Basarab, D. Kouame, and J.-Y. Tourneret, "Joint bayesian deconvolution and point spread function estimation for ultrasound imaging," in *Proc. IEEE International Symposium on Biomedical Imaging (ISBI)*, New York, USA, April 2015.

[8] R. Morin, A. Basarab, and D. Kouame, "Alternating direction method of multipliers framework for super-resolution in ultrasound imaging," in *Proc. IEEE International Symposium on Biomedical Imaging (ISBI)*, Barcelona, Spain, May 2012, pp. 1595–1598.

[9] J. Sun, J. Sun, Z. Xu, and H.-Y. Shum, "Image super-resolution using gradient profile prior," in *Proc. IEEE Conference on Computer Vision and Pattern Recognition (CVPR)*, 2008, pp. 1–8.

[10] N. Zhao, Q. Wei, A. Basarab, D. Kouame, and J.-Y. Tourneret, "Fast single image super-resolution," 2015. [Online]. Available: http://arxiv.org/abs/1510.00143

[11] M. D. Robinson, C. A. Toth, J. Y. Lo, and S. Farsiu, "Efficient Fourier-Wavelet super-resolution," *IEEE Trans. Image Process.*, vol. 19, no. 10, pp. 2669–2681, 2010.

[12] Q. Wei, N. Dobigeon, and J.-Y. Tourneret, "Fast fusion of multi-band images based on solving a Sylvester equation," *IEEE Trans. Image Process.*, 2015, to appear.

[13] O. Féron, F. Orieux, and J.-F. Giovannelli, "Gradient scan Gibbs sampler: an efficient algorithm for high-dimensional Gaussian distributions," 2015. [Online]. Available: http://arxiv.org/abs/1509.03495

[14] C. Chaux, P. L. Combettes, J.-C. Pesquet, and V. R. Wajs, "A variational formulation for frame-based inverse problems," *Inv. Prob.*, pp. 1495–1518, 2007.

[15] N. Zhao, A. Basarab, D. Kouamé, and J.-Y. Tourneret, "Joint segmentation and deconvolution of ultrasound images using a hierarchical Bayesian model based on generalized Gaussian priors," 2015. [Online]. Available: http://arxiv.org/abs/1412.2813

[16] O. Michailovich and D. Adam, "Robust estimation of ultrasound pulses using outlier-resistant de-noising," *IEEE Trans. Med. Imag.*, vol. 22, no. 3, pp. 368–381, 3 2003.